


HUMAN IRIS CLASSIFICATION THROUGH HISTOGRAM OF ORIENTED GRADIENT FEATURES WITH VARIOUS DISTANCE METRICS

Arnab Mukherjee¹ , Md. Zahidul Islam²  and Lasker Ershad Ali^{3,*} 

¹*Department of Quantitative Sciences (Mathematics),*

International University of Business Agriculture and Technology, Dhaka, Bangladesh

²*School of Engineering, Design and Built Environment,*

Western Sydney University, Kingswood, Australia

³*Mathematics Discipline, Khulna University, Khulna, Bangladesh*

**Corresponding author: Lasker Ershad Ali (ershad@math.ku.ac.bd)*

Abstract Human iris classification remains an active research area in the fields of biometrics as well as computer vision. In iris biometrics, most of the visible or near-infrared (NIR) eye images suffer from multiple noise sources, and the dispersive spectrum changes hugely. These changes occur due to spattering, albedo, and spectrum absorbance selectively. However, accurate iris classification for distance images is still a challenging task. To solve it effectively, we propose a machine learning (ML)-based iris classification employing a dense feature extraction method with various distance metrics. More specifically, this learning model focuses on the Histogram of Oriented Gradients (HOG) descriptor and K-Nearest Neighbour (K-NN) classifier with various distance metrics. The HOG descriptor has some advantages for this proposed distant-based iris classification, for example, insensitive to multiple lighting and noises, shift invariance, capacity to tolerate iris variations within the classes, etc. Additionally, this study investigates the most reliable distance metric that is less affected by different levels of noise. A publicly accessible CASIA-V4 distance image database is conducted for the experimental evaluation. To evaluate the performance of the classification models, we consider different measures such as recall, precision, F_1 -score, and accuracy. The reported results are tabulated as well as optimized through Receiver Operating Characteristic (ROC) curves. The experimental results demonstrate that the Canberra distance metric with low dimensional HOG features provides better recognition accuracy (90.55%) compared to other distance metrics.

Keywords: iris classification, image gradient, Histogram of Oriented Gradient features, distance metrics, confusion matrix, ROC curves.

1. Introduction

Iris recognition is a cutting-edge biometric technique that recognizes or confirms the identity of a person swiftly and efficiently by performing a set of mathematical operators on the stored biometric characteristics. Besides, physical contact is completely absent here to isolate iris images and analyze their patterns because this identification process is completely non-invasive. As a result, the demands for reliable security in offline and online authentications are constantly growing. In our networked society, biometric technologies have a variety of applications namely, ATM card authentication, e-commerce,

banking, access control to restricted zones, border-crossing, access to control computers, database access control in distributed systems, verification of suspects in crowds at airports and stations, identification of missing children, law enforcement activities and so on [34]. Without specific tools or automatic machine-learning techniques, it is very tough for a human operator to maintain high-security surveillance in these cases at a distance.

Nowadays the security fields follow different types of technologies to verify individual identities. Token-based and knowledge-based methods are two traditional ways of identifying an individual. The knowledge-based identifiers like personal identification numbers (PINs), usernames, and passwords can be forgotten or guessed by a third party. The token-based identifiers, for example, driver's licenses, passports, smart cards, ATM cards, and identification cards may be stolen or lost [39]. Recently, several studies have demonstrated that biometric traits are the most reliable and accurate authentication systems than conventional knowledge-based and token-based techniques. Even if it cannot be forgotten, stolen, or borrowed, and practically, forging is not possible. Among various physical traits, the iris has more advantages over other fingerprints, faces, eyes, ears, retina, DNA, palm print recognition, etc. [38]. Since iris is an externally visible internal organ that is highly protected from varied environmental conditions. It has unique patterns for an individual that are not related to any genetic factor. Iris texture has a high degree of randomness and individuality and remains unchanged from the age of three through the whole life, which is observed through the clinical evidence in [16]. In real life, there is no chance of a person having the right and left iris patterns or identical twins, or even two human iris textures being identical [38]. The above characteristics make it a promising biometric trait to verify and authenticate individual identities. However, this biometric technology has only been utilized in highly secure applications for government and civil society because of real-time constraints. Though the iris is a visible biometric characteristic like an eye, face, or finger, it is not as easy to recognize as those recognitions due to environmental conditions. The camera distances make it more challenging to capture clear iris texture during eye image acquisition. Capturing eye images in controlled or under less controlled conditions affects the quality of iris images greatly because of uncontrolled light sources. Under less controlled environments, the eye images captured at long distances with near-infrared imaging have multiple sources of noises, for instance, partial eye images, eyelids, glasses, eyelashes, defocus blur, etc., as illustrated in the Fig. 1. These types of noises demote drastically the image quality, pose difficulties in depicting distinct iris textures, and influence the further stages. In a controlled environment, the quality of eye images is high due to capturing at a close distance.

The previous attempts were only focused on close-distant images with controlled environments and global feature descriptors like wavelet filters. Those descriptors cannot extract the below-mentioned enormous iris patterns. Even, the local intensity color

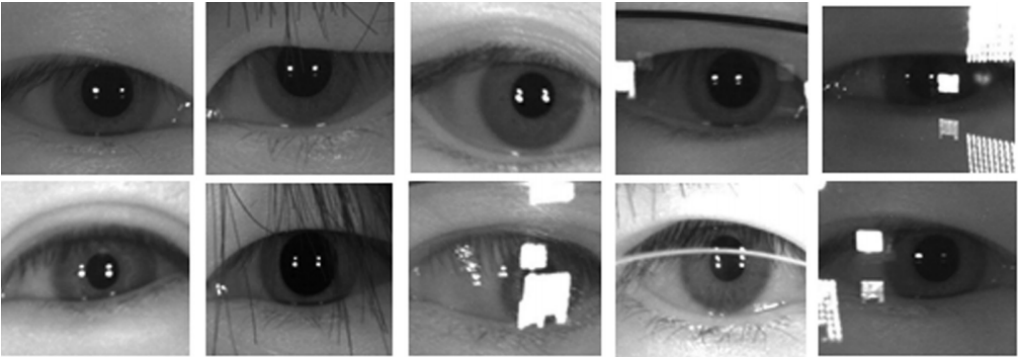


Fig. 1. Long-range eye images from CASIA-v4 database.

density, and pixel position of an image are not utilized there. While iris textures provide high distinctiveness, freckles, wrinkles, a variety of colors, zigzag patterns, etc. [3]. In reality, these features of various forms like textural, structural, and statistical features are highly required to recognize an individual at a distance. This work emphasizes block-based representation of local image contrast to overcome the limitations of wavelet filters. Herein, image gradient characterizes the structure or shape of iris patterns using local intensity gradient distributions and edge detection. More specially, the gradient features pool the edge orientations into small spatial regions to retrieve both micro-structures and macro-structures of iris patterns.

To consider the iris's textural characteristics and imaging conditions, this paper proposes a Histogram of Oriented Gradient feature descriptors to retrieve the spatial characteristics strategically from the local illumination variations of an iris image. The next stage is to explore a classifier that can recognize swiftly the iris features, which have the lowest implications on a variety of noises as well as enhance the classification performance. The classification stage perfect for a distance-based classifier because of being our experimental database imbalance [21,35]. The instances of minority subjects/classes are often sparse and scattered in imbalanced datasets and the majority subjects dominate the feature space. Consequently, misclassifications may occur as a result of higher distances between the instances of minority subjects and lower distances between the majority subjects. To address this issue, it is urgent to investigate deeply the influence of choosing various distance metrics during the classification of a large number of real-time images. For example, Euclidean distance is effective for numerical features like weight, height, salary, etc., that have equal importance over the continuous feature space. While Manhattan distance works effectively with categorical or binary feature points like DNA sequences. Manhattan distance is less affected by outliers compared to Euclidean distance. In this perspective, the mix of categorical and numerical features for

each type can be handled by the K-Nearest Neighbour classifier (K-NN) with a weighted distance metric. A perfect distance metric aids in the learning of the input iris patterns by computing the similarity between iris images and concluding informative decisions. The primary objective of the work is to consistently overcome existing shortcomings and find a supervised algorithm for remote iris recognition in less constrained environments.

The following sections organize the rest of this work: Section 2 reviews a few recent studies on the iris. Section 3 designs the architectural diagram of the iris classification approach. Experimental settings and evaluations are done sequentially in section 4. A statistical analysis is given graphically in section 5. Lastly, a brief conclusion is provided in section 6.

2. Related works

This section reviews a few recent research findings that are very similar to image gradient and distance-based iris recognition. The integrated stages of effective iris recognition are eye image capturing, iris region segmentation, normalization, feature extraction, classification, and iris recognition. The initial stage of eye image acquisition faces various challenges, for example, low resolution, off-axis, blur, motion, occlusion, and specular reflections in real-time environments and degrade the further processes [26]. Specialized, hybrid, and deep learning methods are enlisted to address these challenges [2]. Specialized methods use prior information about iris shape like annular iris/ elliptical shape, and dark area of the pupil. The iris trait features are identified unambiguously in the iris image [11, 15, 43]. These methods are fast without training images and effective for high-quality constrained iris images but not for completely unconstrained irises. Hybrid methods combine the specialized methods with ML algorithms to enhance iris segmentation performance [19, 32, 33, 42]. The ML algorithms produce coarse segmentation, and then a specialized approach is employed to generate the desired segmentation. The hybrid method adjusts these ML algorithms relying on the training process and the conditions of iris images. They can be more accurate due to employing iris priors and ground truth but not fast like specialized methods. However, these approaches are not enough to meet the challenges that arise in unconstrained iris images as still those are heavily dependent on iris priors. Recently, deep learning methods [2, 36, 47], follow semantic segmentation methods to alleviate the influence of unreliable iris priors. These methods provide more accuracy compared to previous methods as well as do not need to handcrafted features. Typically, they are slower due to tuning more parameters, required large-scale training data, and high computational cost.

The earlier approaches were developed based on wavelet filters and distance metrics for iris recognition. The drawbacks of these works are to ensure equal good-quality eye images from constraint environments [3]. Also, the recognition performance reduces significantly due to noisy artifacts, visible iris images, uncontrolled light sources, etc.

Pourreza et al. [7]. noticed that most of the wavelet transforms cannot extract spatial information practically and introduced contourlet transform to address such issues.

Tan and Kumar devised several approaches in [22,23,43,44] to deal with the existing problems for both visible and near-infrared imaging. Among them, the integration of integrating fragile bit [18] and weight map methods [12] through a weighted sum technique obtained the highest accuracy of 93.8% on the CASIA-V4 distance database.

Li et al. provided a weighted histogram of co-occurrence phases to extract the characteristics of local iris texture [25]. Bhattacharyya distance matched these distinctive and insensitive phase histograms with varying levels of illumination and noises. To overcome the challenge of matching low-resolution probe iris images with high-resolution enrolled iris images, Liu et al. developed a metric learning system [27]. The process has been carried out by learning the Mahalanobis distance and measuring appropriate pairwise similarities on the training set to minimize the divergence between the learned matching results and ideal matching outcomes.

The above-mentioned methods lost distinctive information on iris images due to environmental challenges and iris texture deformation. Ali et al. modified the contrast-limited adaptive histogram to alleviate the loss of information that helps to retrieve informative characteristics with speeded-up robust feature descriptor [4]. The proposed SURF-based algorithm achieved 99% and 99.5% recognition accuracy for left and right irises respectively using the CASIA-V4 distance database. Additionally, they noticed that fusion rule selection influences the classification performance at a certain level. The prior wavelet descriptor cannot account for singularities along lines or curves. To capture two-dimensional singularities, Ali et al. designed a feature-level fusion that concatenates the gradient, contourlet, Log-Gabor wavelet, and deep features with equal dimension [5]. The simple feature concatenation shows robustness against different physical challenges. To get over the drawbacks of wavelet and contourlet transforms, Ali et al. developed the Log-Gabor wavelet-based contourlet transform [6]. The merged descriptor extracts the edge and texture information in a variety of directions more compactly than the Log-Gabor or contourlet transform. The concept of remote iris recognition was first presented by Fancourt et al. for high surveillance. The eye images were captured at a 10-meter distance from the acquisition device and obtained an accuracy of 95-100% taking only 50 iris images [14]. Umer et al. retrieved the coarse and spatial properties of iris texture patterns efficiently using textural edges descriptors [46]. The recognition rate of the linear support vector machine (SVM) was 95% with k-fold cross-validation on the UBIRIS.v1 dataset.

Most of the feature-level fusions cannot integrate the discriminative iris patterns efficaciously with optimizing fused features of multimodal approaches due to a lack of homogeneity, adaption, and flexibility. To address these problems, Zhang et al. adopted an adaptive weighted sum method to concatenate the periocular and iris features for enhancing recognition performance [48]. In real-life situations, it is automatically learned

by neural networks to find out the optimum weights of iris-periocular fusion. Severo et al. proposed an approach that can encompass the iris region as the delimitation of the smallest squared bounding box [40]. This approach retrieves firstly multi-scale features of the iris and then a multi-SVM classifier utilizes the concatenation of HOG and cell mean intensity features. Recently, a few authors have focused on different types of Fourier transform (FT) for enhancement, analysis, restoration, and compression. FT decomposed the iris image into its sine and cosine components, which are considered as features. The authors in [17] evaluate the effects of applying principal component analysis (PCA) on FT except for accurate iris segmentation and feature properties using three distance metrics. Among the distance metrics, Manhattan distance achieved the highest accuracies of 96% and 94% for FT and PCA approaches using only 300 iris images of 50 persons from the CASIA-v1.0 database [2018].

Tarhouni et al. integrated the Fourier histograms of uniform local binary patterns (LBP) and pyramid histograms of gradient magnitudes through PCA [13]. The experiments show a promising result for challenging the CASIA-v4 database by mitigating the effects of the noisy artifacts from multiple sources like reflections, illumination variations, obstacles, and so on. Szymkowski adopted discrete fast FT components selected by PCA to describe iris texture [41]. The database was composed of 510 iris images from CASIA-IrisV4 and the reported average accuracies were 82.8% for K-NN, 86.6% for SVM, and 78.7% for ANN classifiers. The drawbacks of all the Fourier transforms are sensitivity to noise, boundary effects, and computationally intensive, especially for multi-dimensional images, which lead to retrieving inaccurate iris features. Arnab et al. introduced the local adaptive threshold method and k means clustering based color image segmentation to consider background clutter, changes in scale, partial occlusions, illumination, and color variation, which are common phenomenons for distant images [20, 28]. The author also developed a human identification scheme using an oriented autocorrelation feature descriptor and correlation distance classifier. The method performs effectively for distant captured iris images with losing shift-invariance but shows robustness against various noisy artifacts, rotation, occlusion, and illumination variation challenges [31].

As discussed above, remote iris classification is still very challenging for visible and near-infrared imaging at a distance in the fields of biometrics. The aim of combining HOG and K-NN with various distances is to find an appropriate balance that can overcome those shortcomings. Hope, this work contributes to selecting the perfect distance metric for further studies depending on the specific characteristics of data points, especially distance-based algorithms. This work is motivated by the computational simplicity of HOG descriptor [10], the robustness of various distance metrics in [29, 31], and the gradient strengthens against local illumination changes, etc.

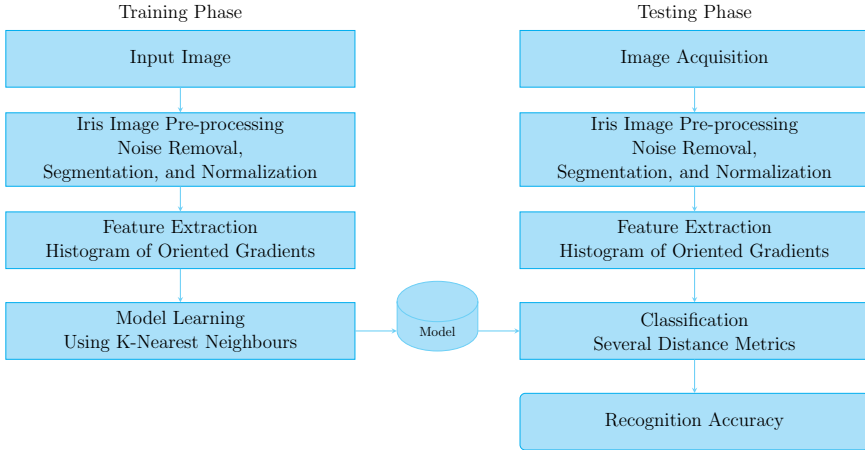


Fig. 2. The proposed architectural framework.

3. Methodology

This section provides a summary of the suggested machine learning algorithm, which integrates the HOG and distance classifier. Firstly, a reflection removal technique, a single-scale retinex algorithm is adopted to suppress the influence of different reflections. Secondly, the annular iris is separated using a random walker scheme from an eye image with low computational complexity. Thirdly, the segmented iris image is remapped by Daugman's rubber sheet model into a fixed dimension i.e., iris normalization to make a direct comparison between the iris images. Then, the images are sent to the automated HOG descriptor to extract distinctive iris patterns as feature vectors. Finally, the recognition accuracy is attained using the extracted feature vectors as input to the distance classifier. In the training phase, the model learns to train from the training images, and its performance is measured in the testing phase using test images. The architectural framework depicts the iris recognition system consecutively in Fig. 2.

3.1. Image pre-processing

Non-uniform illumination is a familiar phenomenon for distantly acquired eye images in real environments caused by uncontrolled light sources and multiple sources of noise. These certain noises create obstacles to separate accurate iris from the eye images. So, iris image pre-processing is required to address these issues. We adopt a single-scale retinex algorithm to improve image quality through high dynamic range compression [42].

Mathematically, the algorithm can be expressed as the following equation.

$$R_{\text{Im}}(p, q) = \log \frac{\text{Im}(p, q)}{G_{\tau} * \text{Im}(p, q)}. \quad (1)$$

Here, $\text{Im}(p, q)$ is a grey scale eye image, $G_{\tau}(p, q) = C \exp[-(p^2 + q^2)/\tau^2]$ is a Gaussian kernel, “*” denotes the convolution operator and $\tau = 1.5$ refers to the standard deviation.

3.2. Iris segmentation

Iris segmentation refers to the scheme of iris localization and separation automatically from the eye images. Due to poor segmentation, the feature descriptor fails to extract iris textures from the less discriminative regions which leads to incorrect iris recognition. The further stages such as feature extraction, classification, and recognition intricately rely on the quality of iris segmentation. To consider those issues, a graph theory-based random walker algorithm is employed to obtain the coarsely segmented binary iris masks in this work. The binary iris masks from the coarse iris segmentation are utilized to know detailed information about the estimation of iris center. The initial center of the iris and pupil is fixed using both the iris image and the corresponding binary mask. After that, the flash-points of papillary and limbic are approximately located with the help of a circular model. The iris segmentation stage is finished after eliminating occlusion noises. To understand more about the random walker segmentation algorithm deeply, the work in [6, 43] might be seen at a glance.

3.3. Iris normalization

The size and shape of the irises may change due to varying imaging distances and rotation of the acquisition device or eye. Illumination variation is also the cause of iris contraction or dilation. So, it is more conducive to removing the dimensional inconsistencies for matching two irises. Once a segment iris image is obtained, we follow the most commonly used Daugman’s rubber sheet model to make up elastic deformation of iris textures [11]. It is performed by re-mapping every pixel $\text{Im}(p, q)$ of the iris region from raw cartesian coordinates (p, q) to a pairwise non-concentric polar coordinates (r, θ) i.e., $r \in [0, 1]$ and $\theta \in [0, 2\pi]$. Mathematically, the re-mapping process may be expressed as:

$$\left. \begin{aligned} \text{Im}(p(r, \theta), q(r, \theta)) &\rightarrow \text{Im}(r, \theta) \\ p(r, \theta) &= (1 - r)p_{\text{pu}}(\theta)r p_{\text{bp}}(\theta) \\ q(r, \theta) &= (1 - r)q_{\text{pu}}(\theta)r q_{\text{bp}}(\theta) \end{aligned} \right\} \quad (2)$$

where $\text{Im}(p, q)$ represents the intensity value of the iris region image at each point (p, q) . The parameters $p(r, \theta)$ and $q(r, \theta)$ denote the co-ordinates of pupil ($p_{\text{pu}}(\theta), q_{\text{pu}}(\theta)$) and iris boundary points ($p_{\text{bp}}(\theta), q_{\text{bp}}(\theta)$) along the θ direction. The outcomes of noise removal from eye images, iris separation, and normalization are illustrated sequentially in Fig. 3.

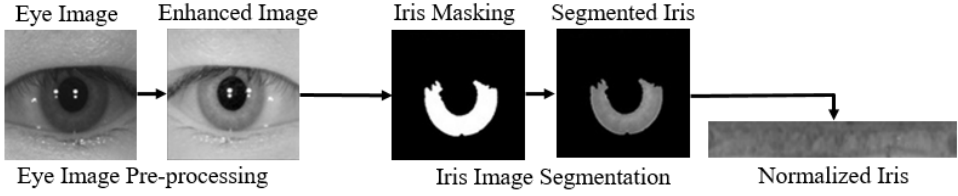


Fig. 3. Iris image pre-processing flow chart.

3.4. Gradient feature extraction

The researchers of INRIA (French National Institute for Research in Computer Science and Automation), Dalal, and Triggs devised the Histograms of Oriented Gradients feature descriptor [10]. This descriptor has been derived from scale-invariant feature transforms, and also parallels edge orientation histograms as well as shape contexts. The details of local object shape and appearance by capturing the edge or gradient structure using regional intensity variations are the primary purpose of this descriptor. Practically, this is done by splitting the localized image into blocks (grid) and each block is subdivided into smaller connected cells. All the locally oriented gradients within the cell are reshaped into a cell histogram. The cell histograms must be locally normalized within a block to account for the variations in illumination and contrast.

In addition, it does not change with photometric and geometric transformations because of local cell operation. The HOG feature scheme follows the steps in a local portion of an image to count the occurrences of oriented gradients.

Step 1: Gradient computation

In an image, the gradient strengths and orientations rely on the local properties of each pixel i.e., directional sub-divided color or intensity. The gradient values are computed along the vertical and horizontal directions by convolving the input image $Im(p, q)$ with 1D centered point discrete derivative masks $D_p = [1 \ 0 \ -1]$ and $D_q = [1 \ 0 \ -1]^T$. If the horizontal and vertical gradients are $G_p(p, q) = Im(p, q) * D_p$ and $G_q(p, q) = Im(p, q) * D_q$, respectively, the gradient magnitude M_G and orientation θ_G will be computed at the point (p, q) as follows:

$$M_G(p, q) = \sqrt{(G_p(p, q))^2 + (G_q(p, q))^2}, \quad (3)$$

$$\theta_G = \tan^{-1}(G_p(p, q)/G_q(p, q)) = \tan^{-1} \left(\frac{\partial G}{\partial q} / \frac{\partial G}{\partial p} \right). \quad (4)$$

Step 2: Orientation binning

The cell histogram is to be constituted in step 2. The 1D histogram is constructed by reshaping the local gradient orientations over the pixels of a cell into angular bins

(ranging from 0 to 360°). The local orientations are assigned to the nearest bins by voting weights for each pixel over the local spatial region, i.e., a cell. Then, the gradient orientations of all pixels $\text{Im}(p, q)$ in a cell α are distributed into N bins. The gradient magnitudes with a gradient angle of $\Delta\theta$ degree are accumulated in the respective bin h_l , which denotes the heights of the bins. Finally, the discretization of orientations into N bins each of $\Delta\theta$ degrees constructs the 1D histogram H_i as follows:

$$H_i = [h_l]_{l=1}^N = \sum_{\text{Im}(p,q) \in \alpha} M_G(p, q); \theta_G(p, q) \in \Delta\theta, \quad (5)$$

where $\Delta\theta = 360^\circ/N$.

Step 3: Block descriptor

Step 3 requires grouping the cell histograms into larger spatial connected blocks F_i .

Step 4: Block normalization

The cell histograms are to be locally normalized within a block for counting the variations in illumination, and contrast [10]. As each block is composed of a group of cells, a cell may be contained in various block normalizations for the overlapping block.

Step 5: Concatenation of histogram features

Finally, the histogram of oriented feature vectors ϑ is constituted by integrating cell histograms across from all the normalized blocks in a sliding window, which represents a one-dimensional array of histograms.

To obtain fixed feature dimensions, the input images must be resized with 64×64 pixels. The size of blocks is set to 2×2 cells and every single cell consists of 8×8 pixels. 9 orientation bins between -180° and $+180^\circ$ (signed gradients) are used to construct histogram bins so that the HOG features can be organized sequentially according to their properties. A total of 49 blocks is computed for an image with 64×64 pixels. The final HOG feature descriptor is formulated as follows:

$$\vartheta = [F_1, F_2, \dots, F_i, \dots, F_{36}], \quad (6)$$

where ϑ denotes the HOG feature descriptor, and F_i is the normalized block vector in i th block. Every block has four cell histograms with nine bins, $F_i = [\bar{h}_{1,i}, \bar{h}_{2,i}, \dots, \bar{h}_{i,j}, \dots, \bar{h}_{36,i}]$, where $\bar{h}_{i,j}$ is the j th normalized value of i th block. The flow diagram of the HOG feature extraction is given systematically in Fig. 4.

3.5. K-Nearest Neighbour classification

K-Nearest Neighbour (K-NN) is a distance-based supervised machine learning algorithm that performs pattern recognition tasks for classifying objects based on various features. It ensures better performance in bio-informatics, data mining, and image classification

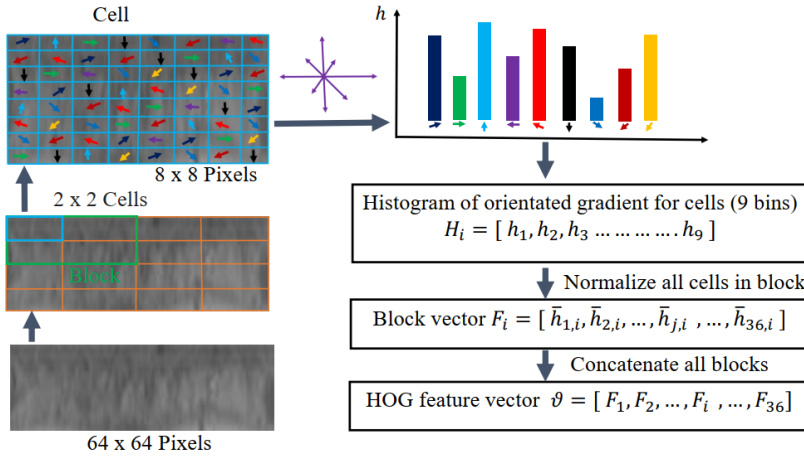


Fig. 4. The flow diagram of HOG feature extraction.

when the features are labeled prior with low dimensionality as well as scaled in equal weight. The main advantage over the other classifiers is that there's no need for pre-training, the model does not learn in the training phase, even needs not to tune more parameters. It also assumes that similar things exist nearby and classifies the test iris images based on the similarity measure of prior stored feature vectors. To supervise the HOG model for such properties, the K-NN algorithm compels us to follow instead of the other classification methods. Besides, K-NN functions as an outlier detector by locating feature points that have few or no neighbours within a fixed radius.

The review section 2 shows that the Euclidean and Hamming distances are used widely in classification problems but in most of the cases, accurate predictions depend on feature properties, distance metrics, and so on. The following metrics are utilized to compare and measure the distances between test and training images [29] as there is no comparative study of distance metrics. Let $p = (p_1, p_2, p_3, \dots, p_n)$ and $q = (q_1, q_2, q_3, \dots, q_n) \in R^n$ be the two feature vectors in n -dimensional space. The distance measure between p and q vectors may be defined as

Euclidean distance (Eucl) It is a straight line distance, which represents the sum of the squared differences of two attribute vectors by taking the square root.

$$D_{\text{Eucl}}(p, q) = \sqrt{\sum_{j=1}^n (p_j - q_j)^2}, \quad (7)$$

where p_j is the j th component in the vector p and q_j is the j th component in the vector q .

Sokalmichener distance (Soka) The distance computes the Sokal-Michener dissimilarity between Boolean 1D arrays p and q . The Boolean array p is a sequence of numerics that consists of 0 (false) and 1 (true) and has no intermediate values. The Boolean 1D arrays with a threshold value and Sokalmichener distance are defined as

$$p = \begin{cases} 1 & \text{if } p_j \geq 0.1667, \\ 0 & \text{if } p_j < 0.1667, \end{cases} \quad (8)$$

$$D_{\text{Soka}}(p, q) = \frac{2(m_{10} + m_{01})}{m_{11} + m_{00} + 2(m_{10} + m_{01})}. \quad (9)$$

Here, m_{xy} counts the number of occurrences of $p_j = x$ and $q_j = y$ for $j < n$, and n defines the total number of points in a feature vector p .

Yule distance (Yule) Yule distance is a measure of dissimilarity between two probability distributions based on their overlap. The Yule dissimilarity is defined as

$$D_{\text{Yule}}(p, q) = \frac{2m_{10}m_{01}}{m_{11}m_{00} + m_{10}m_{01}}. \quad (10)$$

Jaccard distance (Jacc) It is a statistical metric that is generated from the Jaccard index and measures the diversity of iris patterns. The Jaccard dissimilarity between boolean 1D arrays p and q is defined as

$$D_{\text{Jacc}}(p, q) = \frac{m_{10} + m_{01}}{m_{11} + m_{10} + m_{01}}. \quad (11)$$

Dice distance (Dice) The distance is close to the Jaccard index which measures the dissimilarity of two patterns. The Dice dissimilarity between p and q iris vectors is

$$D_{\text{Dice}}(p, q) = \frac{m_{10} + m_{01}}{2m_{11} + m_{10} + m_{01}}. \quad (12)$$

Bray-Curtis distance (Bray) The Braycurtis distance is the absolute differences between two attribute vectors with taking the summation, which differences are divided by their summed attribute values.

$$D_{\text{Bray}}(p, q) = \frac{\sum_{j=1}^n |p_j - q_j|}{\sum_{j=1}^n |p_j| + \sum_{j=1}^n |q_j|}. \quad (13)$$

Canberra distance (Canb) It is an extension of L_1 distance that includes weights and measures the dissimilarity of ranked lists. The sum of absolute differences is divided by their summation between a pair of points over a vector space.

$$D_{\text{Canb}}(p, q) = \sum_{j=1}^n \frac{|p_j - q_j|}{|p_j| + |q_j|}. \quad (14)$$

Manhattan distance (Manh) It is the sum of absolute differences of two opposite attributes over the normed vector space. It is most preferable for high dimensionality and provides more reliable results due to the absolute value of distance.

$$D_{\text{Manh}}(p, q) = \sum_{j=1}^n |p_j - q_j|. \quad (15)$$

Cosine distance (Cosi) This distance measures the angle between two vectors of inner product space with magnitude and is computed from one minus the cosine of the included angle between two attribute vectors.

$$D_{\text{Cosi}}(p, q) = 1 - \frac{\sum_{j=1}^n p_j q_j}{\sqrt{\sum_{j=1}^n p_j^2 \sum_{j=1}^n q_j^2}}, \quad (16)$$

where p_j is the j th value in the vector p and q_j is the j th value in the vector q .

Correlation distance (Corr) Between two feature vectors, the linear relationship is measured in this case by subtracting Pearson's correlation coefficient from one.

$$D_{\text{Corr}}(p, q) = 1 - \frac{\sum_{j=1}^n (p_j - \bar{p})(q_j - \bar{q})}{\sqrt{\sum_{j=1}^n (p_j - \bar{p})^2 \sum_{j=1}^n (q_j - \bar{q})^2}} \quad (17)$$

where \bar{p} is the mean of a feature vector p , i.e., $\bar{p} = \frac{1}{n} \sum_{j=1}^n p_j$ and \bar{q} is the mean of a feature vector q , i.e., $\bar{q} = \frac{1}{n} \sum_{j=1}^n q_j$.

4. Database and experimental setup

In this section, a publicly accessible database of remotely captured face images, CASIA-v4 is employed to conduct all of the experiments. The Chinese Academy of Science's Institute of Automation (CASIA), Beijing, China has provided the database to explore iris-based biometric recognition [45]. The facial images are acquired remotely with the help of near-infrared cameras. The distance is three meters away from the subjects under less controlled environments. The full database comprises 142 subjects including 2567 facial images. First, all right and left eyes were separated from the face images and a total of 5134 eye images were obtained. After that, the imbalanced eye images are categorized into 142 subjects i.e., each subject has not an equal number of images, and most of the subjects include regular-irregular images. From the facial images, all the images of the eye cannot locate or isolate exactly owing to having obstruction of glasses and occlusion of eyelids or eyelashes. We only use the regular iris images of the first 14 subjects for parameter tuning and explore that Canberra distance performs the best. Further experiments are conducted using this distance metric. We selected randomly

3233 images as training data from each of the subjects 15-142 to learn the classification model. Similarly, we select 742 images to evaluate the performance of the model as testing data. All the experiments are conducted by dint of Python 3.7 and MATLAB R2018a (Intel Core i5).

K-NN classifier treats all features equally by default to contribute to the distance calculations. Otherwise, the distance measurement will be dominated by the larger feature points if they are on different scales and ranges. Min-max normalization helps to address this issue without distorting the larger differences of those features. Additionally, weighted distances assign higher weights to privilege the important features. The histogram-oriented gradient features V including training and test features from (6) are normalized with the help of the following equation.

$$V = (\vartheta_j - \vartheta_{min}) / (\vartheta_{max} - \vartheta_{min}), \quad (18)$$

where ϑ_j denotes the j^{th} value of feature vector ϑ with maximum value ϑ_{max} and minimum value ϑ_{min} . Challenges such as data sparsity, distance loss of meaning, overfitting, and increased computation cost arise in high dimensional spaces. Therefore, it is more convenient to lessen the dimensionality of HOG features using PCA without loss of useful information. For this purpose, the PCA transform matrix is obtained from training features and then utilized in test features. These low dimensional, labeled, and scaling features help to train the K-NN model effectively, otherwise affect the majority voting in classification.

4.1. Performance measure

The effectiveness of a classification model may be measured using a variety of assessment indicators. The most often used confusion matrix is utilized to determine the model's accuracy and correctness. Accuracy measures the effectiveness of the classifier by its percentage of samples classified accurately. Classification accuracy is defined by

$$\text{Accuracy} = \frac{\text{Number of accurate classified samples}}{\text{Number of all samples}}. \quad (19)$$

The evaluation systems are designed by calculating the following measures to assess the recognition performance within each class of the database.

- (i) True positives (tp): number of positive (p) predictions that are true (t).
- (ii) True negatives (tn): number of negative (n) predictions that are true (t).
- (iii) False positives (fp): number of positive (p) predictions that are false (f).
- (iv) False negatives (fn): number of negative (n) predictions that are false (f).

Tab. 1. Performance measurement for each distance metric.

Distance Metrics	Avg. Precision	Avg. Recall	F_1 -measure	Accuracy (%)
Euclidean distance	0.7931	0.7647	0.7543	75.70
Sokalmichener distance	0.8452	0.8311	0.8193	82.32
Braycurtis distance	0.8772	0.8535	0.8483	85.02
Canberra distance	0.9190	0.9102	0.9053	90.55
Manhattan distance	0.8564	0.8333	0.8262	82.86
Yule distance	0.8622	0.8397	0.8309	83.53
Jaccard distance	0.8508	0.8363	0.8250	83.13
Dice distance	0.8508	0.8363	0.8250	83.13
Cosine distance	0.7951	0.7623	0.7519	75.70
Correlation distance	0.7966	0.7605	0.7505	75.70

The average precision, recall, and F_1 -measure values and accuracy of a multi-class classification system are defined by

$$\text{Average Precision} = \frac{1}{N_c} \sum_{j=1}^{N_c} \frac{tp_j}{tp_j + fp_j}, \quad (20)$$

$$\text{Average Recall} = \frac{1}{N_c} \sum_{j=1}^{N_c} \frac{tp_j}{tp_j + fn_j}, \quad (21)$$

$$F_1\text{-measure} = \frac{2 \times \text{Precision} \times \text{Recall}}{\text{Precision} + \text{Recall}}, \quad (22)$$

$$\text{Accuracy} = \frac{1}{N_c} \sum_{j=1}^{N_c} \frac{tp_j + tn_j}{tp_j + tn_j + fp_j + fn_j}, \quad (23)$$

where N_c is the number of classes; tp_j , fn_j , fp_j and tn_j are the number of true positive, false negative, false positive, and true negative classifications for class j , respectively. The confusion matrix helps to derive these performance measures, which are illustrated graphically in both predicted and actual classification [30] corresponding to their subjects or classes. The performance of dense HOG descriptor with K-NN classifier is computed for each distance metric by measuring average precision, recall, F_1 -measure, and classification accuracy as enlisted in Table 1.

We observe that Canberra distance metric provides the highest average precision (0.9190), recall (0.9102), F_1 -measure (0.9053), and overall classification accuracy (90.55%) among the 10 distance metrics from the Table 1 in case of using HOG features. It is visible from Fig. 5 that the iris feature vector consists of several criteria such as bi-

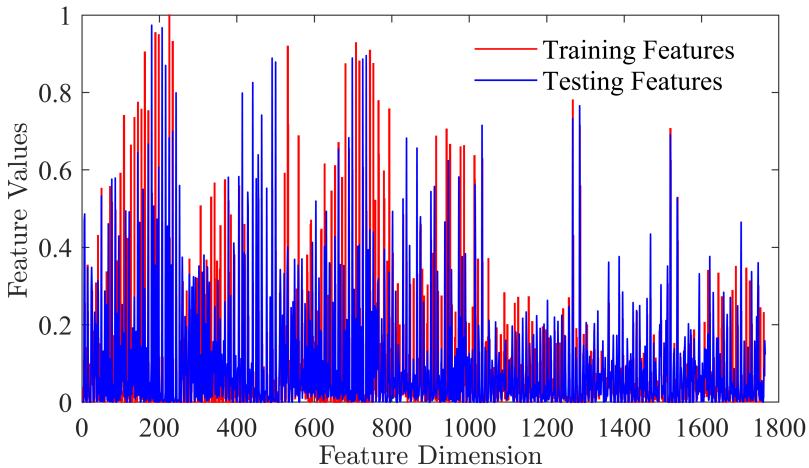


Fig. 5. The HOG feature distribution.

nary features – has any iris shape or not; ordered categorical features – iris shape very densely/iris shape moderately densely/iris shape not densely; numerical features – a measurement like color density in dpi. Canberra Distance utilizes the criteria to recognize the test images in their subjects according to how similar or dissimilar they are with training images. Also, the distance metric deals with mixed types of feature points and sorts the iris features into groups that are more closely or distantly related to each other. Due to appropriate balance, the HOG descriptor shows better performance with the weighted Canberra distance over the other distance metrics.

In addition, we have experimented with edge orientation histograms (EOH), contourlet transform (CT), and uniform gradient local binary patterns (GLBP) features to compare the discriminatory power of HOG features utilizing the Canberra distance metric. These experimental outcomes are enlisted in Table 2 in terms of precision, recall, F_1 -measure, and classification accuracy. It can be found from Table 2 that the Canberra distance-based classification provides the highest result for HOG features compared to the other three feature descriptors. Therefore, it is confident that the HOG descriptor locally extracted more relevant iris textures from the complicated images due to the orientation of the iris image gradient.

4.2. Performance study

This sub-section depicts the performances of feature descriptor as well as the impacts of various parameter selection for optimal classification. The Receiver Operating Characteristic (ROC) curves are plotted concerning false positive rate and true positive rate

Tab. 2. Efficacy of HOG with other feature descriptors.

Feature Descriptors	Avg. Precision	Avg. Recall	F_1 -measure	Accuracy (%)
EOH	0.7129	0.6175	0.6132	61.40
CT	0.7444	0.7107	0.6880	69.63
GLBP	0.8249	0.7818	0.7709	77.32
HOG	0.9190	0.9102	0.9053	90.55

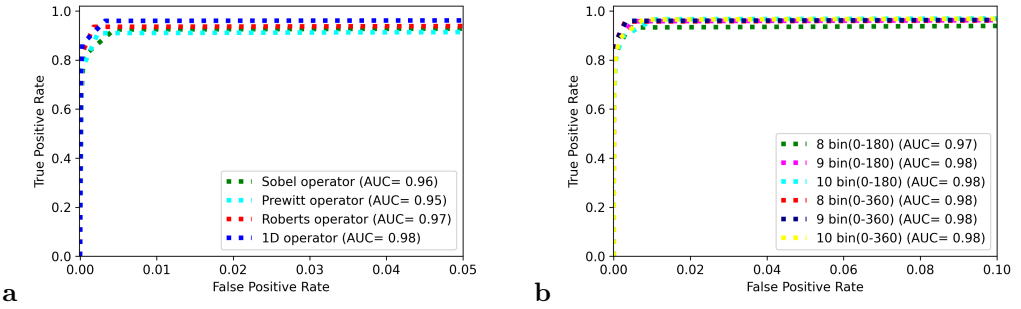


Fig. 6. True versus false positive rates for (a) gradient operators; (b) orientation bins.

with the help of classification threshold values. The performance is indicated by the closed curve to the top-left corner. The study explains the influence of HOG descriptor with the help of ROC curves graphically and confusion matrix from Fig. 6a to Fig. 8a, and obtain the optimal parameters to extract the gradient features like as 64×64 pixels sliding window, one-dimensional derivative masks $[1 \ 0 \ -1]$; 9 orientation bins between -180° and $+180^\circ$ (signed gradients); 2×2 pixel blocks of four 8×8 pixel cells and L_1 -sqrt normalization scheme respectively. The effects of chosen distances are shown not only graphically Figs. 8b, 9a but also numerically in Tables 1, 2.

Gradient computation

Image gradient computation is the first step of retrieving gradient features. Roberts, 1D centered derivatives $[1 \ 0 \ -1]$, Sobel and Prewitt operators are followed to compute image gradient. The one-dimensional derivatives perform best among those operators with the lowest computational cost. The 3×3 Prewitt and Sobel masks reduce the classification performance by around 4% and 5% compared to 1D derivatives. Whereas, the centered 2D derivative masks i.e., 2×2 diagonal Roberts's filter slightly improves the performance by 2% than 3×3 derivative masks. The performances are reduced significantly in Fig. 6a with increasing the size of derivative masks.

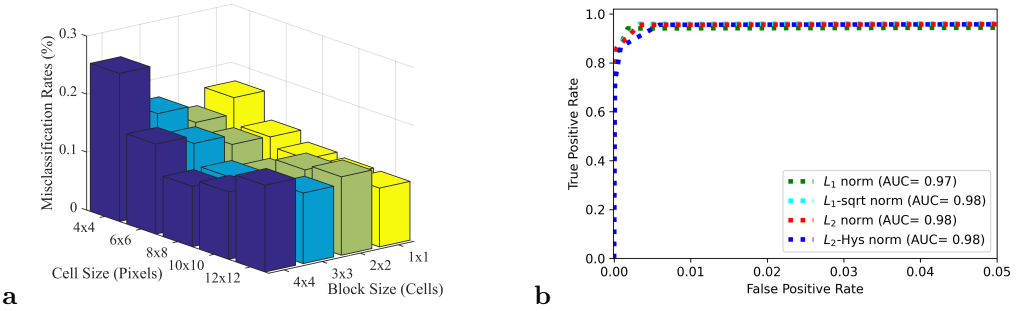


Fig. 7. (a) Misclassification rates. (b) True versus false positive rates for block normalization.

Orientation binning

In the next step, we compute the weighted votes for every pixel to form a histogram based on the oriented vector of iris texture patterns. Then, the computed votes are gathered into orientation bins as cells from the local spatial regions. Regarding rectangular cells, the orientation values of the gradient are evenly spaced in bins between 0° and $+180^\circ$ (unsigned gradients) or between -180° and $+180^\circ$ (signed gradients). The orientation bins of the gradient can be allocated into several bins. The number of orientation bins changes from 8 bins to 10 bins to visualize their performances and the signed gradients of 9 bins perform better among them as shown in Fig. 6b.

Blocks descriptor

The variations of gradient strength occur extensively due to illumination changes and local contrast. So, it is more convenient to find an effective local contrast normalization that contributes to integrating all the cells into larger spatial blocks. Each block normalizes the local contrast individually. We use square R-HOG blocks, which are formulated by $\zeta \times \zeta$ cells per block with $\alpha \times \alpha$ pixels per cell and each cell consists of β orientation bins per cell histogram with the ζ, α, β parameters.

A 3D bar graph is plotted to visualize the misclassification rate for cell size and block size in cells in Fig. 7a. The variation of block sizes is shown with the help of different colors. The 2×2 cell blocks of 8×8 pixel cells work best with a 9.45% misclassification rate among the block descriptors. The 1×1 , 3×3 and 4×4 blocks with their corresponding cells 6×6 , 8×8 perform also good but decrease performance around 1% compared to 2×2 blocks.

Block normalization

The block normalization techniques are adopted for better invariance to illumination and shadowing. If ϑ is the non-normalized feature vector that holds all the histogram of orientations in a block, the normalization schemes $\|\vartheta\|_b$ are defined as (a) L_2 -norm is the square root of the sum of squared values, i.e., $\|\vartheta\|_{b=2} = (\sum_{j=1}^n \vartheta_j^2)^{1/2}$ and L_2 -norm:

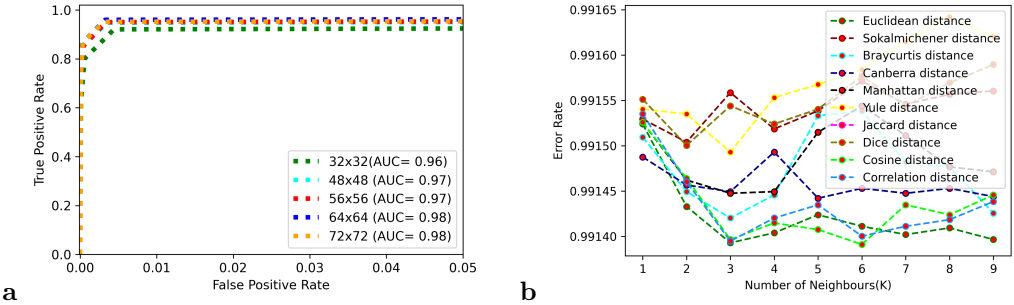


Fig. 8. True versus false positive rates for (a) sliding windows; (b) number of neighbours K.

$v \rightarrow \vartheta / (\|\vartheta\|_2 + \varepsilon)$; (b) L_2 -Hys: $v \rightarrow \vartheta / (\|\vartheta\|_2 + \varepsilon)$, $\vartheta \leq 0.2$; (c) L_1 -norm is the sum of absolute values i.e., $\|\vartheta\|_{b=1} = \sum_{j=1}^n |\vartheta_j|$ and L_1 -norm: $v \rightarrow \vartheta / (\|\vartheta\|_1 + \varepsilon)$ and (d) L_1 -sqrt: $v \rightarrow \vartheta / \sqrt{\|\vartheta\|_1 + \varepsilon}$. Figure 7b shows that L_1 -sqrt and L_2 -norm provide almost similar performance but L_2 -norm reduces performance by 0.27%. Whereas, L_1 – sqrt increases performance significantly by 1.76% and 1.08% than the L_2 -Hys and L_2 -norms. Extensive experiments are carried out to measure the optimal value of ε over a wide range and conclude that there are no more effects of the constant ε on overall results.

Sliding window

The variations of sliding windows pose difficulties in the feature extraction stage and influence the classification results greatly as the computational simplicity relies on sliding windows at large. Figure 8a reports that the performances of sliding window increase up to about 64×64 pixels but decrease performance with 72×72 pixels window. Among them, a window of 64×64 pixels produces a substantial amount of context to recognize iris patterns. The other sliding windows are seen the same on the ROC curves but their evaluation matrices are different. The sliding window 32×32 , 48×48 , 56×56 and 72×72 pixels reduces performance 7.42%, 1.35%, 1.49% and 0.27% respectively on the recognition accuracy due to a lack of sufficient contextual information.

Number of K neighbours

The K parameter refers to the number of nearest neighbours to be considered while making the prediction. This affects the sensitivity of the algorithm to local patterns in the feature space. A smaller K leads to low bias but increases the impact of outliers with complexity and makes the model more prone to overfitting. Whereas, the model arises with less complexity with a larger K, which assists in avoiding overfitting but ignores potential local patterns. The odd number of K defines always a majority class that helps to decide the predicted class. It is clear from Fig. 8b that the 3 nearest neighbours show better performance with the highest value by avoiding ties in voting. The figures of Jaccard and Dice distance overlap due to having similar properties that are assumed

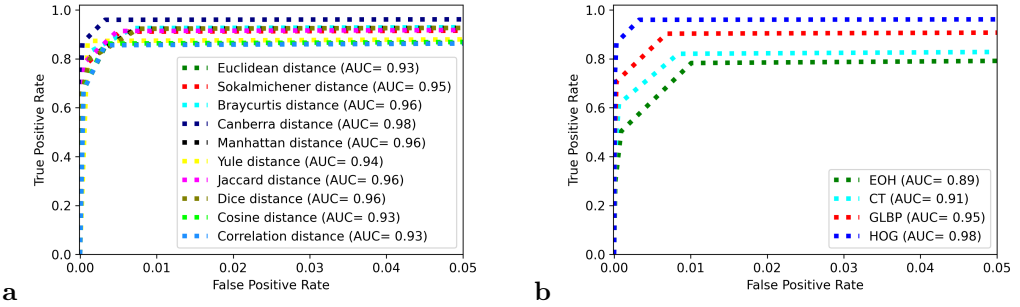


Fig. 9. True versus false positive rates for (a) distance metrics; (b) feature descriptors.

from the measurements in Table 1. It is also visible that there is no optimal value of K , which performs equally well for all the distances. Fig. 8b ensures that the choice of distance metric affects the classification performance significantly but not the selection of the right K in K -NN.

Distance metrics

In this study, the above-mentioned distance metrics are employed to investigate, which distance is less affected by the noise implications. We obtain the optimal performance with the highest outcome (90.55%), while the Canberra distance is applied to train the model instead of mostly using Euclidean and Hamming distance metrics.

The K -NN classifier with Euclidean, Cosine, and Correlation distances reduces performance by around 15% compared to Canberra distance. Although the accuracies of Jaccard and Dice distances are almost the same, the recognition performance is different as shown in Fig. 9a. Seemingly, the Yule distance shows poor performance on ROC curves but its accuracy is so much better than Manhattan, Sokalichener, and Jaccard distances in Table 1. The comparative study suggests that Canberra distance may be an effective metric for gradient feature classification with the highest possible accuracy.

Feature descriptors

A feature descriptor is an algorithm that extracts only the most informative features of an object in terms of a set of numbers. We compare the performance of the dense descriptor HOG with EOH, CT, and GLBP feature descriptors using the Canberra distance-based classifier. These descriptors focus on the shape or structure of iris patterns as they utilize the magnitude and orientations of the gradient to extract features. They provide several computation costs because of extracting various feature properties and measuring the distance between the feature points. Among these descriptors, the HOG feature-based technique classifies the iris images more swiftly than others. The EOH descriptor reduces performance by around 19% consuming huge run time. It is visible from Fig. 9b that

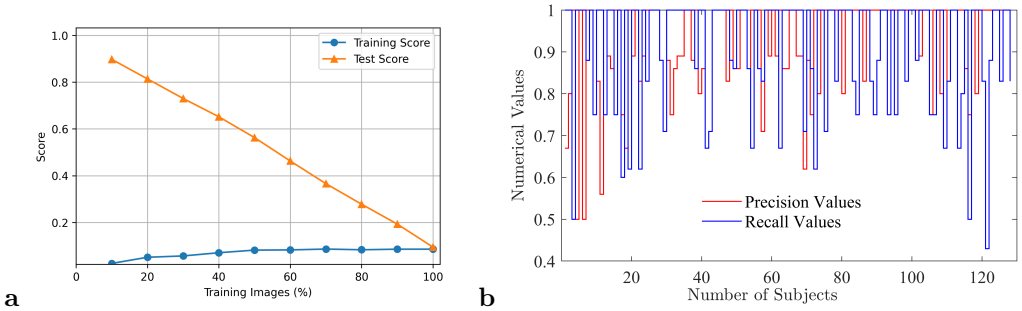


Fig. 10. (a) Plot of K-NN learning curves using HOG features. (b) Subject-based precision-recall curves.

there is a scarcity of threshold points to make the ROC curve smoother because of the imbalance of subjects in training and test sets.

5. Statistical analysis

We assess the performance of the HOG feature descriptor by dint of learning curves and precision-recall curves for every subject concerning their values that are accomplished by the K-NN classifier with Canberra distance. The learning curves show the robustness of the model as well as the scope of using a large number of images in real-life applications. The precision-recall curves interpret the types of noisy images and illustrate the complexity of images within each subject of a database.

In this study, the learning curves diagnose the model's learning and generalization behavior to make a marginal decision. The above yellow and blue learning curves are plotted by using the Canberra distance-based K-NN classifier with the histogram of oriented features. The test score (yellow curve) shows how well the model fits new data, whereas the training score (blue curve) shows how well the model fits the training set. In the beginning, the large gap between the training and test performance shows that the model is under-fitting, which is probably due to the small size of images and database from different distributions. With the increasing of training images, the curves are going to converse a satisfactory score as shown in Fig. 10a. The training scores are enhanced through the iterations of up to 50 percent of training images. After that, those scores are constant and the HOG model fails to obtain 100% accuracy in the training phase while the test scores are increasing and converse to the highest possible score in the end. The learning curves demonstrate that the testing scores could be made better by increasing training images and making the dataset balanced.

Figure 10b plots the precision and recall curves for each subject concerning precision and recall values. The blue color is used for the precision curve, while the red color is

Tab. 3. Performance evaluation with existing cutting-edge approach

Proposed Approaches	Accuracy
Symlet wavelet filter and Spearman distance [29]	80.00%
Principal Component Analysis and Braycurtis distance [37]	80.00%
Level set and local binary pattern with Manhattan distance [9]	81.45%
Discrete fast Fourier transform and Braycurtis distance [41]	82.80%
Radon Transform and Euclidean distance [8]	84.17%
Uniform LBP and Euclidean distance [24]	84.77%
LBP and Euclidean distance [38]	84.88%
GLCM and Euclidean distance [1]	85.00%
CNN feature descriptor and Euclidean distance [5]	86.94%
Contourlet Transform and Hamming distance [7]	88.00%
Histogram of Oriented Gradients and Canberra distance – Proposed	90.55%

used for the recall curve. We can see that 51 subjects in precision curves and 48 subjects in recall curves cannot attain the maximum values due to having a variety of obstacles such as eyelids, eyelashes, illumination, and internal eye variations in these subjects. The images of 46 subjects within 128 subjects and 672 images among the 742 test images are classified accurately, while 70 images of the rest subjects are not recognized by their corresponding subjects. For example, the 18th and 29th subjects have the lowest recall value of (0.50) and the 17th subject has the lowest precision value of (0.50), indicating that some but not all of the subjects' test images are recognized. In practice, the images of these 82 subjects are imbalanced and contain several noises during the acquisition process, which impede an illustration of clear iris textures. For weak segmentation of irises, the HOG descriptor cannot retrieve relevant features and learn robustly from those iris textures. Thus, the K-NN model fails to classify the complicated iris images accurately and does not obtain overall 100% recognition accuracy. The performance scores of the F_1 -measure are overlapping, which indicates that the feature distributions are irregular in these subjects. In the other subjects, the high success rates of evaluation metrics show that the models are successful in iris image classification.

Table 3 provides a comparison with earlier approaches including the reported results. Few of these techniques examined the performance of classification on various types of databases with various numbers of training and test images. For instance, Tan and Kumar only performed their experiments using the first 8 right or left eye images from the CASIA-v4 distance database [45]. The overall recognition accuracy was 93.90% employing training images from the first 10 subjects and test images from subjects 11-141. The recognition rate of Chan method was 90.43% considering 79 training images

from the 10 subjects and 961 test images from the remaining 131 subjects from the proposed database [23].

It is remarkably worthy that the authors in [5] reported several efficiencies in adopting multi-feature descriptors. The accuracy of 98.17% is the highest among the outcomes, however, their performances are not explicitly comparable to our work. Because the authors not only considered iris images but also included contextual eye images having pupil, eyelash, eyelid, sclera, and so on. Therefore, the experimental results of the proposed framework would not be feasible to make a comparison with other experimental outcomes directly. We employ 3975 images including 3233 images for training and 742 images for testing; and also do not consider the regular eye images of the first 14 subjects. It is clear from Fig. 1 that our experimental database consists of more complicated and non-linear images than others.

However, the supervised approach is better as compared to existing methods concerning near-infrared distance iris images having various illumination conditions and multiple sources of noise. Also, accurate iris segmentation, informative features with lower dimensionality, distance metric of lowest noise implications, and computational simplicity can be considered measurable parameters of good classification performance. Finally, the comparative studies validate that the Canberra distance metric may be applied in the lieu of most widely used Euclidean or Hamming distance metric for noisy datasets and distance-based approaches.

6. Conclusion and future work

This paper has introduced an image gradient and distance-based machine learning algorithm for remote iris recognition. The HOG descriptor captures intuitively the shape of structures in the region by capturing information about gradients. The discriminative power of HOG is to extract successively both microstructures and macro structures of iris patterns from the local contrast and illumination variations. To classify the imbalanced iris images, a weighted distance classifier is needed to explore which is less affected by different levels of noise. Like other classifiers, K-NN is prone to become biased towards the majority of instances of training features but can be handled effectively with the help of weighted Canberra distance. The distance metric emphasizes the larger differences between the iris features and outliers and is more robust to outliers than other distance metrics. The experimental evaluation demonstrates that Canberra distance provides the highest possible classification accuracy (90.55%) with the lowest noise implications.

The combination of HOG and K-NN classifier shows its robustness against local contrast, illumination changes, and occlusions. It is regarded as one of the most influential machine learning algorithms because all the parameters are intricately connected. Though the HOG descriptor extracts the iris features efficiently while retaining robustness to irrelevant variations resulting from environmental changes, it lost shift-invariance

and additivity. The concept of correlation will be adopted in self-similarity to address these issues. It will exploit the spatial and orientational auto-correlations from the local image gradient that prioritize the closer iris patterns in its local neighbourhoods. In the future, a proximity-weighted evidential K-NN classifier will be applied to give more priority to the instances of minority subjects or classes.

References

- [1] E. Acar. Extraction of texture features from local iris areas by GLCM and iris recognition system based on KNN. *European Journal of Technic*, 6(1):44–52, 2016. <https://api.semanticscholar.org/CorpusID:209081348>.
- [2] S. Ahmad and B. Fuller. Unconstrained iris segmentation using convolutional neural networks. In: *Computer Vision – Proc. 14th Asian Conference on Computer Vision (ACCV) 2018 Workshops*, vol. 11367 of *Lecture Notes in Computer Science*, pp. 450–466, 2019. doi:10.1007/978-3-030-21074-8_36.
- [3] A. S. Al-Waisy, R. Qahwaji, S. Ipson, S. Al-Fahdawi, and T. A. Nagem. A multi-biometric iris recognition system based on a deep learning approach. *Pattern Analysis and Applications*, 21(3):783–802, 2018. doi:10.1007/s10044-017-0656-1.
- [4] H. S. Ali, A. I. Ismail, F. A. Farag, and F. E. A. El-Samie. Speeded up robust features for efficient iris recognition. *Signal, Image and Video Processing*, 10:1385–1391, 2016. doi:10.1007/s11760-016-0903-8.
- [5] L. E. Ali, J. Luo, and J. Ma. Iris recognition from distant images based on multiple feature descriptors and classifiers. In: *Proc. 2016 IEEE 13th International Conference on Signal Processing (ICSP)*, pp. 1357–1362. IEEE, 2016. doi:10.1109/ICSP.2016.7878048.
- [6] L. E. Ali, J. Luo, and J. Ma. Effective iris recognition for distant images using log-gabor wavelet based contourlet transform features. In: *Proc. 13th International Conference on Intelligent Computing Theories and Application (ICIC)*, vol. 10361 of *Lecture Notes in Computer Science*, pp. 293–303, 2017. doi:10.1007/978-3-319-63309-1_27.
- [7] A. Azizi and H. R. Pourreza. A new method for iris recognition based on contourlet transform and non linear approximation coefficients. In: *Emerging Intelligent Computing Technology and Applications – Proc. 5th International Conference on Intelligent Computing (ICIC)*, vol. 5754 of *Lecture Notes in Computer Science*, pp. 307–316, 2009. doi:10.1007/978-3-642-04070-2_35.
- [8] B. V. Bharath, A. S. Vilas, K. Manikantan, and S. Ramachandran. Iris recognition using radon transform thresholding based feature extraction with gradient-based isolation as a pre-processing technique. In: *Proc. 2014 9th International Conference on Industrial and Information Systems (ICIIS)*, pp. 1–8, 2014. doi:10.1109/ICIINFS.2014.7036572.
- [9] B. Connor and K. Roy. Iris recognition using level set and local binary pattern. *International Journal of Computer Theory and Engineering*, 6(5):416–420, 2014. doi:10.7763/IJCTE.2014.V6.901.
- [10] N. Dalal and B. Triggs. Histograms of oriented gradients for human detection. In: *Proc. 2005 IEEE Computer Society Conference on Computer Vision and Pattern Recognition (CVPR'05)*, vol. 1, pp. 886–893, 2005. doi:10.1109/CVPR.2005.177.
- [11] J. Daugman. How iris recognition works. In: A. Bovik, ed., *The Essential Guide to Image Processing*, chap. 5, pp. 715–739. Elsevier, 2009. doi:10.1016/B978-0-12-374457-9.00025-1.

- [12] W. Dong, Z. Sun, and T. Tan. Iris matching based on personalized weight map. *IEEE Transactions on Pattern Analysis and Machine Intelligence*, 33(9):1744–1757, 2011. doi:10.1109/TPAMI.2010.227.
- [13] W. El-Tarhouni, A. Abdo, and A. Elmegeisi. Feature fusion using the Local Binary Pattern Histogram Fourier and the Pyramid Histogram of Feature fusion using the Local Binary Pattern Oriented Gradient in iris recognition. In: *Proc. 2021 IEEE 1st International Maghreb Meeting of the Conference on Sciences and Techniques of Automatic Control and Computer Engineering (MI-STA)*, pp. 853–857, 2021. doi:10.1109/MI-STA52233.2021.9464473.
- [14] C. Fancourt, L. Bogoni, K. Hanna, Y. Guo, R. Wildes, et al. Iris recognition at a distance. In: *Proc. 5th International Conference on Audio-and Video-Based Biometric Person Authentication (AVBPA)*, vol. 3546 of *Lecture Notes in Computer Science*, pp. 1–13. Springer, 2005. doi:10.1007/11527923.1.
- [15] A. Gangwar, A. Joshi, A. Singh, F. Alonso-Fernandez, and J. Bigun. IrisSeg: A fast and robust iris segmentation framework for non-ideal iris images. In: *Proc. 2016 International Conference on Biometrics (ICB)*, pp. 1–8. IEEE, 2016. doi:10.1109/ICB.2016.7550096.
- [16] L. George and E. Saad. Iris recognition based on the low order norms of gradient components. *International Journal of Computer and Information Engineering*, 8(8):1240–1246, 01 2014. <https://publications.waset.org/9999069.pdf>.
- [17] M. H. Hamd, S. K. Ahmed, et al. Biometric system design for iris recognition using intelligent algorithms. *International Journal of Modern Education and Computer Science*, 10(3):9–16, 2018. doi:10.5815/ijmecs.2018.03.02.
- [18] K. P. Hollingsworth, K. W. Bowyer, and P. J. Flynn. The best bits in an iris code. *IEEE Transactions on Pattern Analysis and Machine Intelligence*, 31(6):964–973, 2009. doi:10.1109/TPAMI.2008.185.
- [19] Y. Hu, K. Sirlantzis, and G. Howells. Improving colour iris segmentation using a model selection technique. *Pattern Recognition Letters*, 57:24–32, 2015. doi:10.1016/j.patrec.2014.12.012.
- [20] M. Z. Islam, S. Nahar, S. S. Islam, S. Islam, A. Mukherjee, et al. Customized K-Means clustering based color image segmentation measuring PRI. In: *Proc. 2021 International Conference on Electronics, Communications and Information Technology (ICECIT)*, pp. 1–4. IEEE, 2021. doi:10.1109/ICECIT54077.2021.9641094.
- [21] M. E. Kadir, P. S. Akash, S. Sharmin, A. A. Ali, and M. Shoyaib. A proximity weighted evidential k nearest neighbor classifier for imbalanced data. In: *Advances in Knowledge Discovery and Data Mining – Proc. 24th Pacific-Asia Conference (PAKDD)*, vol. 12085 of *Lecture Notes in Computer Science*, pp. 71–83, 2020. doi:10.1007/978-3-030-47436-2.6.
- [22] A. Kumar and T.-S. Chan. Iris recognition using quaternionic sparse orientation code (QSOC). In: *Proc. 2012 IEEE Computer Society Conference on Computer Vision and Pattern Recognition Workshops (CVPRW)*, pp. 59–64, 2012. doi:10.1109/CVPRW.2012.6239216.
- [23] A. Kumar, T.-S. Chan, and C.-W. Tan. Human identification from at-a-distance face images using sparse representation of local iris features. In: *Proc. 2012 5th IAPR International Conference on Biometrics (ICB)*, pp. 303–309, 2012. doi:10.1109/ICB.2012.6199824.
- [24] C. Li, W. Zhou, and S. Yuan. Iris recognition based on a novel variation of local binary pattern. *The Visual Computer*, 31(10):1419–1429, 2015. doi:10.1007/s00371-014-1023-5.
- [25] P. Li, X. Liu, and N. Zhao. Weighted co-occurrence phase histogram for iris recognition. *Pattern Recognition Letters*, 33(8):1000–1005, 2012. doi:10.1016/j.patrec.2011.06.018.
- [26] Y.-H. Li, W. R. Putri, M. S. Aslam, and C.-C. Chang. Robust iris segmentation algorithm

- in non-cooperative environments using interleaved residual U-Net. *Sensors*, 21(4):1434, 2021. doi:10.3390/s21041434.
- [27] J. Liu, Z. Sun, and T. Tan. Distance metric learning for recognizing low-resolution iris images. *Neurocomputing*, 144:484–492, 2014. doi:10.1016/j.neucom.2014.05.016.
- [28] B. Madhu, A. Mukherjee, M. Z. Islam, G. Mamun-Al-Imran, R. Roy, et al. Depth motion map based human action recognition using adaptive threshold technique. In: *Proc. 2021 5th International Conference on Electrical Information and Communication Technology (EICT)*, pp. 1–6, 2021. doi:10.1109/EICT54103.2021.9733611.
- [29] A. Mukherjee, M. Z. Islam, G. Mamun-Al-Imran, and L. E. Ali. Iris recognition using wavelet features and various distance based classification. In: *Proc. 2021 International Conference on Electronics, Communications and Information Technology (ICECIT)*, pp. 1–4, 2021. doi:10.1109/ICECIT54077.2021.9641118.
- [30] A. Mukherjee, M. Z. Islam, R. Roy, and L. E. Ali. Block-based local binary patterns for distant iris recognition using various distance metrics. *International Journal of Image, Graphics and Signal Processing*, 16(3):83–99, 2024. doi:10.5815/ijigsp.2024.03.07.
- [31] A. Mukherjee, K. S. N. Ripon, L. E. Ali, Z. Islam, and G. Mamun-Al-Imran. Image gradient based iris recognition for distantly acquired face images using distance classifiers. In: *Computational Science and Its Applications – Proc. ICCSA Workshops*, vol. 13381 of *Lecture Notes in Computer Science*, pp. 239–252, 2022. doi:10.1007/978-3-031-10548-7_18.
- [32] H. Proenca. Iris recognition: On the segmentation of degraded images acquired in the visible wavelength. *IEEE Transactions on Pattern Analysis and Machine Intelligence*, 32(8):1502–1516, 2010. doi:0.1016/j.dsp.2017.02.003.
- [33] A. Radman, N. Zainal, and S. A. Suandi. Automated segmentation of iris images acquired in an unconstrained environment using HOG-SVM and GrowCut. *Digital Signal Processing*, 64:60–70, 2017. doi:10.1016/j.dsp.2017.02.003.
- [34] K. S. N. Ripon, L. E. Ali, N. Siddique, and J. Ma. Convolutional neural network based eye recognition from distantly acquired face images for human identification. In: *Proc. 2019 International Joint Conference on Neural Networks (IJCNN)*, pp. 1–8, 2019. doi:10.1109/IJCNN.2019.8852190.
- [35] M. Salauddin Khan, T. D. Nath, M. Murad Hossain, A. Mukherjee, H. Bin Hasnath, et al. Comparison of multiclass classification techniques using dry bean dataset. *International Journal of Cognitive Computing in Engineering*, 4:6–20, 2023. doi:10.1016/j.ijcce.2023.01.002.
- [36] M. Sardar, S. Banerjee, and S. Mitra. Iris segmentation using interactive deep learning. *IEEE Access*, 8:219322–219330, 2020. doi:10.1109/ACCESS.2020.3041519.
- [37] Y. Sari, M. Alkaff, and R. A. Pramunendar. Iris recognition based on distance similarity and PCA. In: *Human-Dedicated Sustainable Product and Process Design: Materials, Resources, and Energy: Proc. 4th International Conference on Engineering, Technology, and Industrial Application (ICE-TIA) 2017*, vol. 1977(1) of *AIP Conference Proceedings*, p. 020044, 2018. doi:10.1063/1.5042900.
- [38] S. N. Sarode and A. M. Patil. Iris recognition using LBP with classifiers-KNN and NB. *International Journal of Science and Research*, 4(1):1904–1908, 2015. <https://www.ijsr.net/getabstract.php?paperid=SUB15735>.
- [39] M. Savoj and S. A. Monadjemi. Iris localization using circle and fuzzy circle detection method. *International Journal of Computer and Information Engineering*, 6(1):91–93, 2012. <https://publications.waset.org/1468.pdf>.
- [40] E. Severo, R. Laroca, C. S. Bezerra, L. A. Zanlorensi, D. Weingaertner, et al. A benchmark for iris location and a deep learning detector evaluation. In: *Proc. 2018 International Joint Conference on Neural Networks (IJCNN)*, pp. 1–7, 2018. doi:10.1109/IJCNN.2018.8489638.

- [41] M. Szymkowski, P. Jasiński, and K. Saeed. Iris-based human identity recognition with machine learning methods and discrete fast fourier transform. *Innovations in Systems and Software Engineering*, 17:309–317, 2021. doi:10.1007/s11334-021-00392-9.
- [42] C.-W. Tan and A. Kumar. Unified framework for automated iris segmentation using distantly acquired face images. *IEEE Transactions on Image Processing*, 21(9):4068–4079, 2012. doi:10.1109/TIP.2012.2199125.
- [43] C.-W. Tan and A. Kumar. Towards online iris and periocular recognition under relaxed imaging constraints. *IEEE Transactions on Image Processing*, 22(10):3751–3765, 2013. doi:10.1109/TIP.2013.2260165.
- [44] C.-W. Tan and A. Kumar. Accurate iris recognition at a distance using stabilized iris encoding and Zernike moments phase features. *IEEE Transactions on Image Processing*, 23(9):3962–3974, 2014. doi:10.1109/TIP.2014.2337714.
- [45] T. Tan and Z. Sun. CASIA Iris Image Database. <http://biometrics.idealtest.org/#/datasetDetail/4>, V. 4 [Accessed: 2018-06-16].
- [46] S. Umer, B. C. Dhara, and B. Chanda. An iris recognition system based on analysis of textural edginess descriptors. *IETE Technical Review*, 35(2):145–156, 2018. doi:10.1080/02564602.2016.1265904.
- [47] C. Wang, J. Muhammad, Y. Wang, Z. He, and Z. Sun. Towards complete and accurate iris segmentation using deep multi-task attention network for non-cooperative iris recognition. *IEEE Transactions on Information Forensics and Security*, 15:2944–2959, 2020. doi:10.1109/TIFS.2020.2980791.
- [48] Q. Zhang, H. Li, Z. Sun, and T. Tan. Deep feature fusion for iris and periocular biometrics on mobile devices. *IEEE Transactions on Information Forensics and Security*, 13(11):2897–2912, 2018. doi:10.1109/TIFS.2018.2833033.

Arnab Mukherjee received a B.Sc. degree (Hons.) in Mathematics and M.Sc. degree in Applied Mathematics from the Mathematics Discipline, Khulna University, Khulna, Bangladesh, in 2018 and 2020, respectively. He is currently working as a Lecturer of Mathematics under the Department of Quantitative Sciences, International University of Business Agriculture and Technology, Dhaka, Bangladesh. He has several research articles published in internationally accredited journals and conferences. He is researching the applications of artificial intelligence for high-security surveillance. His research interests include computer vision, especially statistical learning and information intelligence, data science, image processing, biometric recognition, machine learning algorithms, deep learning, and applied mathematics.

Md. Zahidul Islam completed his B.Sc. (Hons.) in Mathematics in 2019 and also completed his M.Sc. in Applied Mathematics in 2021 from the Mathematics Discipline, Khulna University, Khulna, Bangladesh. Currently, he is doing Ph.D. in the School of Engineering, Design, and Built Environment at Western Sydney University, Australia. His research interests include image processing, artificial intelligence, machine learning, deep learning, neural networks, infrastructure, computer vision, and applied mathematics.

Dr. Lasker Ershad Ali received a Bachelor of Science (B.Sc.) degree in Mathematics and a Master of Science (M.Sc.) degree in Applied Mathematics from Khulna University in 2006 and 2008, respectively. He also received a Doctor of Natural Science degree from Peking University in 2018. After working as a Lecturer (from 2008), an Assistant Professor (from 2010), and an Associate Professor (from 2015), he has been a Professor of Mathematics at Khulna University since 2019. Currently, he is supervising several undergraduate and postgraduate students and conducting some projects as a principal investigator and a co-investigator. He has authored or coauthored around 40 publications in different conferences and peer-reviewed journals. His research interests include biometrics recognition, pattern recognition, signal and image processing, machine learning, deep learning, artificial intelligence, computer vision, and applied mathematics. He is a life member of the Bangladesh Mathematical Society (BMS).